Phase locking and noise-driven dynamics in a Josephson-junction electronic analog

Aeron McConnell,* Sara Idris,* Brian Opatosky, and François Amet†
Department of Physics and Astronomy, Appalachian State University, Boone, North Carolina 28608, USA

(Received 31 July 2021; revised 1 November 2021; accepted 8 November 2021; published 22 November 2021)

We present an electronic circuit whose dynamical properties emulate those of a resistively and capacitively shunted Josephson junction. We show how it reproduces the switching properties of a shunted junction and its dependence on the quality factor. A thermal noise source is then used to characterize the temperature dependence of the phase dynamics. In the presence of an AC drive, phase locking is observed at integer and rational multiples of the drive frequency, and it competes with chaotic behavior when the quality factor of the junction exceeds unity. We characterize the stability of phase-locked and chaotic states in the presence of thermal noise.

DOI: 10.1103/PhysRevB.104.184513

I. INTRODUCTION

Josephson junctions consist of two superconducting electrodes separated by a weak link [1,2]. The supercurrent flowing through a junction depends on the superconducting phase difference ϕ between the two electrodes. The electronic properties of a junction largely result from the dynamical properties of $\phi(t)$, which are equivalent to those of a driven nonlinear oscillator. In fact, within the resistively and capacitively shunted junction model (RCSJ) [3,4], ϕ follows a differential equation which is identical to that of a driven, damped, rigid pendulum.

While the phenomenology of Josephson junction dynamics has been well established experimentally, a considerable amount of information is lost in typical transport measurements since they cannot measure the time evolution of the phase $\phi(t)$ directly. For example, a measurement of the I-V curve of a Josephson junction yields only information on the time average of the phase derivative $\dot{\phi}$, which is proportional to the voltage, but barely provides any information about the frequency spectrum of $\phi(t)$.

Electronic circuits relying on mainstream components can emulate the exact same dynamical system, but on timescales that are more conducive to time-dependent phase measurements. They thus provide a convenient way to simulate the properties of Josephson junctions as predicted by the RCSJ model. Such Josephson junction analogs were proposed in Refs. [5–12] and typically rely on voltage-controlled oscillators. Prior work also demonstrated how analog circuits can help characterize noise-driven dynamics [13], such as a thermally activated escape rate from a potential well [14]. However, to our knowledge this approach has not been used to investigate the effect of thermal noise on the phase dynamics of a Josephson junction. Further, our simulations produce results with much higher resolution than much prior analog research has yielded due to general advancement in technological capacity.

In this work, we probe some of the common properties of Josephson junctions using an analog circuit. Our setup allows us to directly measure $\dot{\phi}(t)$ before time averaging. We can therefore extract valuable insights into the frequency spectrum of the junction's phase while exploring the parameter space of the RCSJ model. We first determine the switching properties of the analog junction and its dependence on the quality factor. The addition of thermal noise to the circuit allows the observation of phase diffusion in overdamped junctions, as well as the thermally activated premature switching of underdamped junctions. In the presence of an AC drive, we observe the AC Josephson effect [2,15] and its dependence on the Q factor of the junction, as well as the power and frequency of the AC drive. To that end, we directly measure the frequency spectrum of $\dot{\phi}(t)$ and show how it depends on the presence of integer and fractional phase locking. Using the same technique, we discuss the onset of chaos in such systems and the thermal stability of phase-locked and chaotic states. Overall, this analog system provides a simple, room-temperature setup to predict phase dynamics and help design circuits based on Josephson junctions.

II. DESCRIPTION OF THE CIRCUIT

A. Main circuit

A simplified schematic of the circuit is shown on Fig. 1(a). It is inspired by Ref. [12], and it relies on a voltage-controlled oscillator (VCO) whose sinusoidal output V_2 has an amplitude α and a frequency which is proportional to the input voltage. The VCO is in the feedback loop of the circuit; therefore, its input is actually the output of the operational amplifier V_{out}, so $V_2 = \alpha \sin(2\pi k \int V_{\text{out}} dt)$. A constant input voltage V_{out} therefore results in a sinusoidal output of frequency kV_{out}.

We characterize the VCO in greater detail in the Supplemental Material [16]. If we define $\dot{\phi} \equiv 2\pi k V_{\text{out}}$, we obtain the following differential equation for ϕ:

$$\ddot{\phi} + \frac{\omega_0}{Q}\dot{\phi} + \omega_0^2 \sin\phi = \omega_0^2 \frac{V_b}{V_c}. \quad (1)$$

*These authors contributed equally to this work.
†ametf@appstate.edu

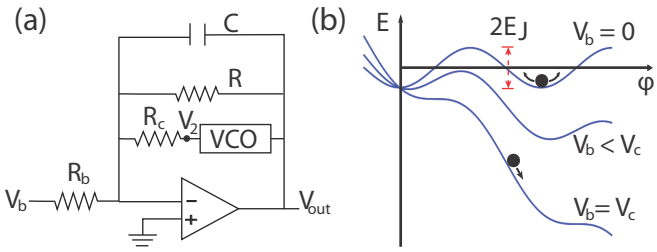

FIG. 1. A simplified representation of the circuit is shown in (a), with the most relevant components labeled. (b) gives an idealized diagram of washboard potentials at varying bias currents.

Here, the junction's frequency is defined as $\omega_0^2 \equiv \frac{2\pi\alpha k}{R_c C}$, the quality factor $Q \equiv RC\omega_0$, and the critical voltage $V_c \equiv \frac{-\alpha R_b}{R_c}$. A more detailed derivation of this result is provided in the Supplemental Material [16], and we show how to determine Q and ω_0 experimentally. This equation is similar to the familiar RCSJ model for the phase of a current-biased Josephson junction [2–4]. The effective potential associated with the dynamical properties of this phase is shown on Fig. 1(b) and is given by:

$$U(\phi) = -E_J\left(\cos(\phi) + \frac{V_b}{V_c}\phi\right). \tag{2}$$

Here, E_J is the analog of the Josephson energy in the RCSJ model and is defined as $E_J \equiv \frac{\alpha}{2\pi k R_c}$. For our circuit, this quantity is on the order of 80 nJ, which is, of course, many orders of magnitude greater than the energy scale for a real junction. Details on the derivation of this result are provided in the Supplemental Material [16].

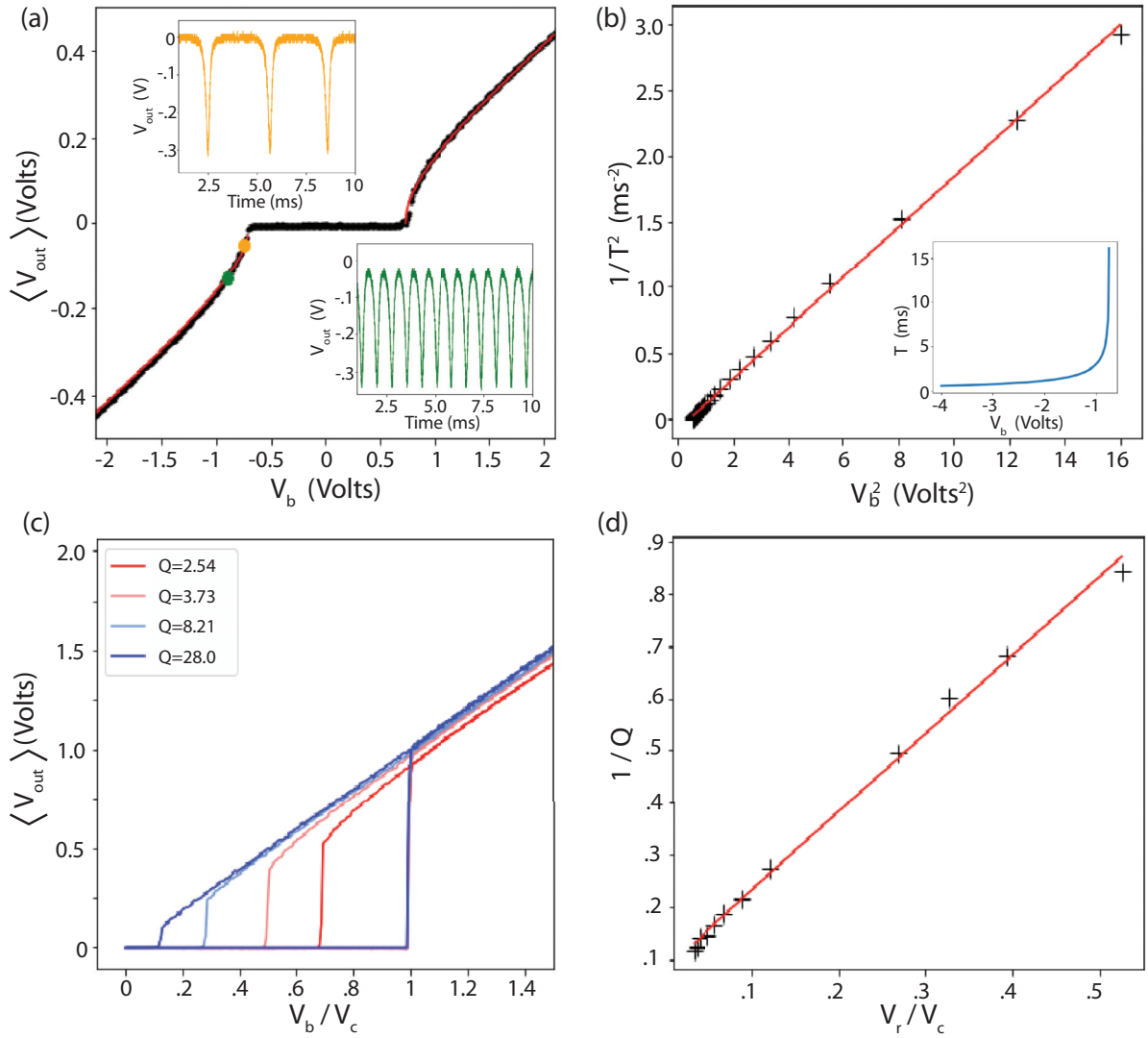

FIG. 2. Switching dynamics. (a) $\langle V_{out} \rangle$ measured as a function of the DC bias voltage for an analog junction with $Q = 0.6$. The red curve is a fit to the RCSJ model prediction [Eq. (3)]. Insets: $V_{out}(t)$ before time averaging measured at bias values shown by yellow and green dots on the main curve. The period of oscillation clearly increases closer to the critical voltage. (b) $1/T^2$ plotted as a function of V_b^2, which is expected to be linear according to Eq. (4). A fit, shown in red and relying on Eq. (4), yields a junction period $T_0 = 2.1$ ms. Inset: $T(V_b)$ using the same data. (c) I-V curves measured for different quality factors. The retrapping voltage decreases at larger Q values. (d) Given the RCSJ model's prediction that $V_r/V_c \propto 1/Q$, the values of $1/Q$ versus V_r/V_c were plotted for 12 different Q values to show this proportionality.

Note that the bias voltage V_b plays the role of what is usually the current bias in the RCSJ model. In what follows, we will therefore refer to switching, retrapping, and critical voltages instead of currents. Curves representing $V_{\text{out}}(V_b)$ will be referred to as I-V curves to follow the standard terminology.

In our setup, the bias voltage is the sum of three components: DC and AC voltages, as well as a random voltage source that emulates thermal noise and is described later.

B. Switching dynamics

Figure 2(a) shows an example of an I-V curve obtained when the analog junction is nearly overdamped with a Q factor of 0.6. Here, V_{out} is time averaged by a low-pass filter with a time constant of 82 ms. As the bias exceeds the critical voltage, V_{out} becomes finite, which corresponds to the normal state in the RCSJ model. In the overdamped case, the junction's I-V curve is not hysteretic, so the switching and retrapping voltages are identical [2]. The red curve corresponds to a fit to the RCSJ model's prediction in the overdamped case:

$$V_{\text{out}} = \pm \frac{f_0 Q}{k} \sqrt{\left(\frac{V_b}{V_c}\right)^2 - 1}. \tag{3}$$

The two insets in Fig. 2(a) represent $V_{\text{out}} \propto \dot{\phi}$ before time averaging. As the bias exceeds the critical voltage, the phase runs down the tilted washboard potential with an angular velocity that decreases whenever ϕ goes over a local maximum of $U(\phi)$. This results in an oscillation of $\dot{\phi}$, which is shown as an inset in Fig. 2(a). As the bias approaches the critical voltage, the period of those oscillations diverges, as shown in the insets in Figs. 2(a) and 2(b). Indeed, in the overdamped case, the period T of those oscillations is expected to follow [3,4]:

$$T = \frac{T_0}{Q\sqrt{\left(\frac{V_b}{V_c}\right)^2 - 1}}. \tag{4}$$

This trend is shown in Fig. 2(b), where T^{-2} is plotted as a function of V_b^2, showing a linear trend, as expected from Eq. (4). The red fit corresponds to a period $T_0 \approx 2.1$ ms (using $Q \approx 0.6$).

Changing the value of R modifies the quality factor of the analog junction, which can be tuned to the underdamped regime. As expected, the I-V curves become more hysteretic as the quality factor increases. When $V_b > V_s \approx V_c$, the system starts to rapidly fall toward lower values of the washboard potential. However, as V_b is decreased, a finite voltage is observed across the junction until the retrapping voltage $V_r < V_s$. Indeed, given the inertia of the system, the tilt of the washboard potential must be brought closer to the horizontal in order to stop the running phase. Figure 2(c) shows normalized I-V curves for four different quality factors. The retrapping current becomes increasingly small deeper in the underdamped regime. Within the RCSJ model the ratio V_r/V_c scales like $4/(Q\pi)$ for $Q \gg 1$ [4]; we therefore plot the ratio V_r/V_c as a function of $1/Q$ in Fig. 2(d) and, indeed, observe a linear trend.

C. Effect of thermal noise

Effective temperature

The effect of finite temperature on the phase dynamics can be emulated by applying Gaussian white voltage noise to the input of the circuit: this requires a random voltage source with a flat frequency spectrum and a normal distribution with zero mean. Using the standard expression for Johnson-Nyquist noise, this emulates an effective temperature: $k_B T_{\text{eff}} = \langle v_{\text{rms}} \rangle^2 / 4BR$, where B is the bandwidth of the noise.

We numerically generate a random array of voltage values with a Gaussian white noise distribution and, using a voltage output digital-to-analog converter (DAC), add it to the DC bias voltage before feeding it to the input of the junction. The effective temperature is then simply varied by adjusting the rms voltage of the white noise. Importantly, since the sampling rate of the DAC is finite (10 kHz), the spectral density of the noise is flat up to only a few kilohertz and starts dropping as it approaches the sampling rate, but this is sufficient in this low-frequency setup to emulate thermal noise. Indeed, the junction frequency f_0 is typically a few hundred hertz. Over the relevant range of frequencies (a few hertz to a few kilohertz), our noise spectral density therefore approximates white noise very well, despite the simplicity of the setup. This allows us to determine the temperature dependence of the phase dynamics in the overdamped and underdamped case.

Around zero bias, phase slips between two local minima of the washboard potential can still occur at finite temperature with a probability that scales like the Boltzmann weight $\exp(-\Delta U/k_B T)$, with $\Delta U = 2E_J$ [17]. This causes the phase to diffuse and a nonzero voltage to develop across the junction even when the bias voltage is below the critical voltage. Figure 3(a) shows $V_{\text{out}}(V_b)$ measured at three effective temperatures for an analog junction whose Q factor is 0.6. The blue, pink, and red curves were obtained when the rms voltage of the noise source was 2.36, 3.19, and 4.67 V, respectively. A finite slope develops around zero bias and increases with temperature. At the highest effective temperature (red curve), the zero-voltage state effectively disappears.

In the presence of phase diffusion, the zero-bias resistance, which in our case corresponds to dV_{out}/dV_b around $V_b = 0$, is known to be thermally activated [18]:

$$\tilde{R} \equiv \left.\frac{dV_{\text{out}}}{dV_b}\right|_{V_b=0} \propto \frac{1}{T} \exp\left(\frac{-2E_j}{k_B T}\right). \tag{5}$$

This implies that $\ln(\tilde{R}T)$ is proportional to $1/T$ with a slope proportional to E_j, which can be represented on an Arrhenius plot, as shown in Fig. 3(b). $\langle V_{\text{out}}(V_b) \rangle$ was measured in the presence of thermal voltage noise with varying rms amplitude. The curves were numerically differentiated to get dV_{out}/dV_b at zero bias. Since the effective temperature is proportional to V_{rms}^2, we plotted the decimal logarithm $\log_{10}(\tilde{R}V_{\text{rms}}^2)$ versus V_{rms}^{-2}, which shows an evident activated behavior in Fig. 3(b). To verify that the slope scaled according to E_j, we changed E_j while keeping Q constant. When we change E_j to 2/3 of its original value, we observe again a thermally activated behavior, but the slope is reduced by a comparable factor of $\approx$0.58.

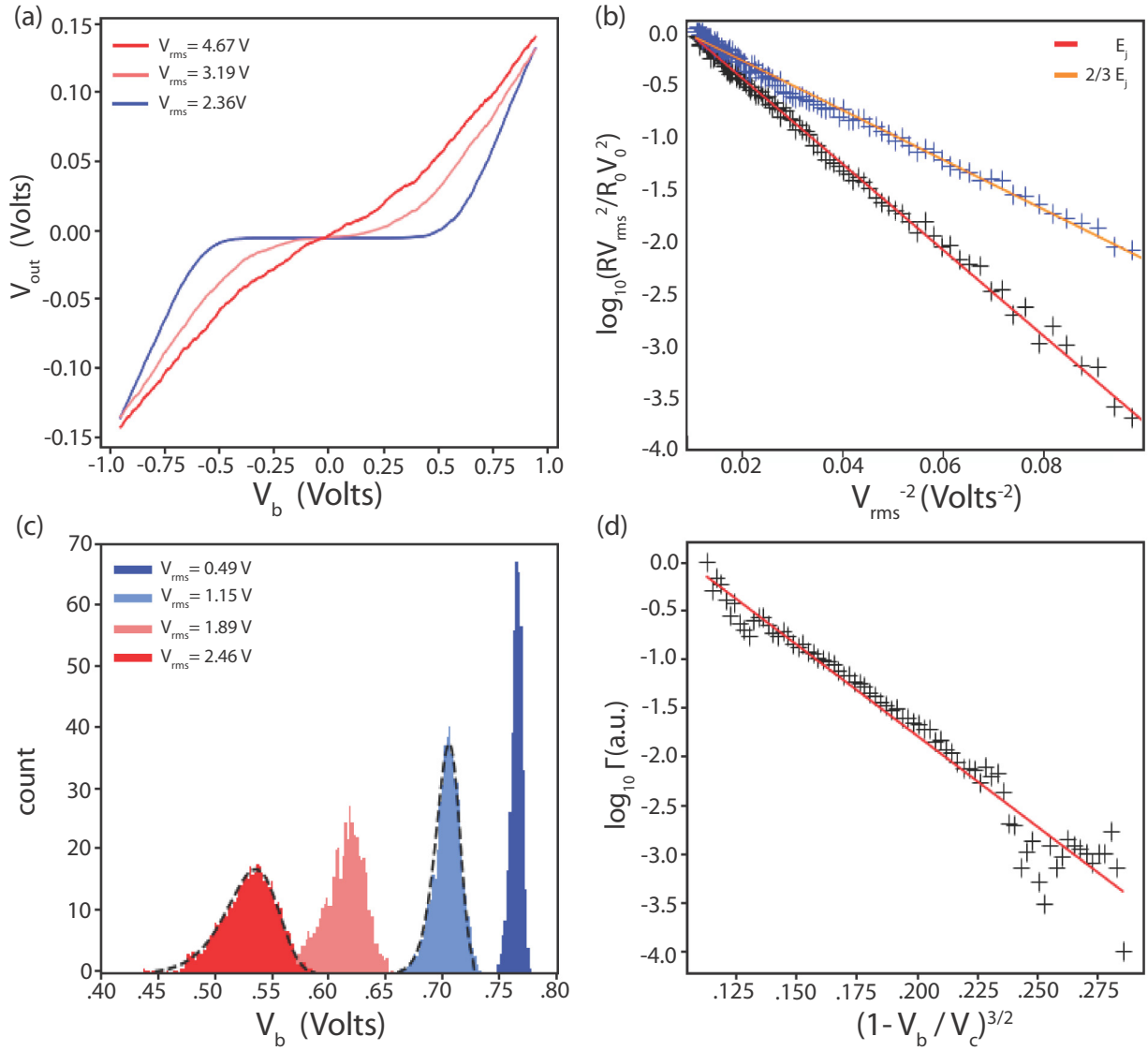

FIG. 3. Thermal noise. (a) Increasing the rms voltage of the noise source causes the superconducting region to start tilting and causes the junction to become slightly resistive, even below the critical voltage. At high enough rms voltages the superconducting behavior is entirely washed out by the thermal noise. (b) Plotting $\log_{10}(\tilde{R}V_{\rm rms}^2)$ versus $V_{\rm rms}^{-2}$, we expect to see linear relationships with slopes proportional to E_J. (c) As the thermal noise rms voltage is increased, the probability distribution of the switching voltage becomes broader, and the mean drops towards lower bias. (d) By considering $\Delta U = 2E_J(1 - V_b/V_c)^{\frac{3}{2}}$, where the switching rate is proportional to $e^{-\Delta U/kT}$, we see that plotting $\log_{10}(\Gamma)$ versus $(1 - V_b/V_c)^{3/2}$ gives a linear relationship which is confirmed in this plot.

In the underdamped case, a phase slip causes the phase to durably escape the zero-voltage state. The barrier height that determines the escape probability is bias voltage dependent and equal to $\Delta U = 2E_J(1 - V_b/V_c)^{\frac{3}{2}}$ [14,19–21]. To determine the switching voltage distribution, 4000 I-V curves were recorded for each effective temperature, wherein the bias voltage was ramped up to record the switching voltage. The distributions of switching voltage values are plotted for four effective temperatures in Fig. 3(c). As the thermal noise rms amplitude is increased, the switching voltage distribution shifts towards lower bias voltages. Additionally, we observe a clear broadening of the switching voltage distribution with temperature, which concurs with the $T^{2/3}$ scaling predicted by the RCSJ model [22].

The probability that switching occurs at a given voltage bias V_b can be expressed in terms of the switching rate Γ and the rate of change of the voltage bias $\dot{v}$ [20,23]:

$$P(V_b) = \frac{\Gamma}{\dot{v}}\left(1 - \int_0^{V_b} P(V)dV\right). \tag{6}$$

We can solve Eq. (6) numerically, assuming a thermally activated switching rate $e^{-\Delta U/kT}$, where $\Delta U = 2E_J(1 - V_b/V_c)^{\frac{3}{2}}$. A least-squares fit allows us to fit the histograms of Fig. 3(c) (dashed black curves) with a dimensionless ratio $\frac{2E_J}{kT} \approx 22.1$ and ≈ 109 (red and light blue histograms, respectively). Note that since $T \propto V_{\rm rms}^2$, that ratio is expected to differ by a factor of ≈ 4.6 between the two distributions, in close agreement with our fit. As a point of comparison, for

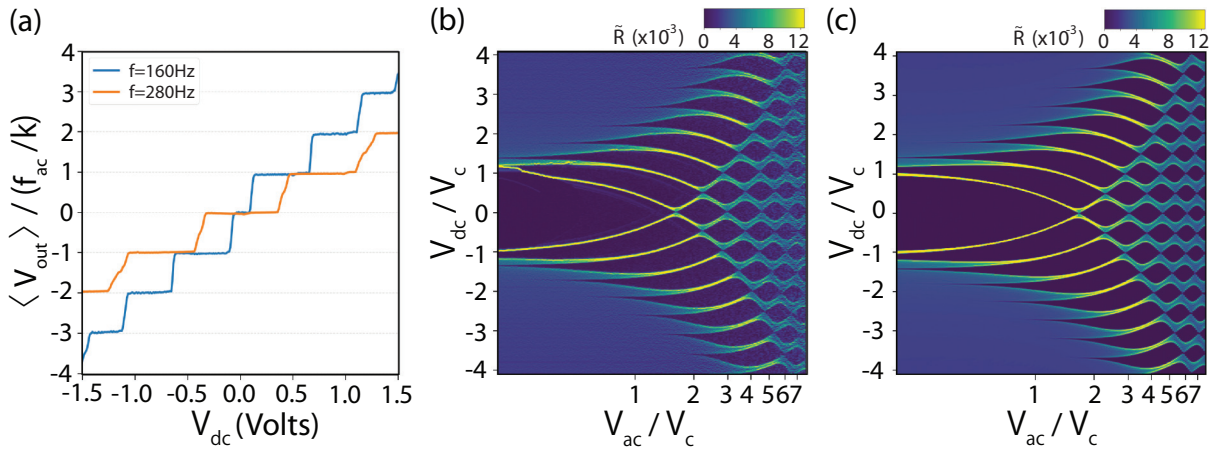

FIG. 4. Inverse AC Josephson effect. (a) Plot of the average junction voltage, normalized in integral multiples of f_{ac}/k versus V_{dc}. (b) Experimentally determined map of differential resistance $\tilde{R}$ in V_b versus V_{ac} space; normalized in units of critical voltage V_c ($\tilde{R}$ is dimensionless). (c) Numerical simulation of (b) via numerical integration of (1).

a Josephson junction with a critical current of 1 μA at 1 K, this ratio would be on the order of 47. It is therefore worth noting that even though E_J, kT, and other energy scales in this system are many orders of magnitude larger than in a typical low-temperature Josephson junction transport experiment, the dimensionless ratios of the activation energies over kT are comparable, and we therefore observe a phenomenology which is very close to what can be observed in a transport measurement.

Finally, Eq. (6) allows the direct calculation of Γ using the switching histograms. Since $\Gamma \propto e^{-\Delta U/kT}$, we represent $\log_{10}(\Gamma)$ as a function of $(1 - V_b/V_c)^{3/2}$ to highlight the bias dependence of the barrier height. Similar to the fits of the red histogram in Fig. 3(c), the linear fit to Fig. 3(d) suggests a ratio $2E_J/kT \approx 22.1$, in agreement with the previously mentioned fit.

III. INVERSE AC JOSEPHSON EFFECT

The inverse AC Josephson effect can appear when a Josephson junction is driven by an AC current [2,11,15]. The dynamics of the current driven case are not analytically solvable [24], but since (1) is equivalent to a damped driven pendulum, qualitative descriptions rooted in this mechanical analog offer useful insights. In the presence of a periodic driving torque, the pendulum can enter a phase-locked state and complete q revolutions during p periods of the torque. This phase-locked state is resilient to small perturbations in the DC torque. The average angular frequency of the pendulum and the drive are therefore commensurate: $\langle\dot{\phi}\rangle = \frac{p}{q}\omega$. In a Josephson junction, the voltage across the junction is $\frac{\hbar\dot{\phi}}{2e}$, so phase locking results in a quantized voltage at rational multiples of $\hbar\omega/2e$. The robustness of the phase-locked state against perturbations allows it to persist over a finite interval of the DC current, which creates voltage plateaus in the I-V curve.

Observation of Shapiro steps

Although this phenomenon is typically observed when Josephson junctions are exposed to microwave radiation, in our case, the junction's frequency f_0 is a few hundred hertz, so the AC drive can be generated by a simple lock-in amplifier. That AC voltage is added to a DC component and supplied to the bias input V_b. The equivalent of the I-V curve, which, as stated previously, in our case is a plot of $V_{out}(V_b)$, is then expected to exhibit Shapiro steps [2,11,15].

Figure 4(a) displays the I-V characteristics of the circuit driven by two different frequencies: one at 160 Hz and one at 280 Hz. I-V curves were collected with a fixed AC driving voltage of 0.75 V and varied DC driving voltage. $\langle V_{out}\rangle$ is plotted against V_{dc} and normalized in units of f_{ac}/k, the value of a voltage step in our setup, where k is the voltage to frequency gain of the VCO and f_{ac} is the driving frequency. This normalization helps visualize the integer quantization and shows the frequency dependence of a voltage step. Note that the different average slopes come from the normalization procedure.

Figure 4(b) displays a map of experimentally measured differential resistance $\tilde{R} \equiv \frac{d\langle V_{out}\rangle}{dV_{dc}}$. The data were collected by measuring $\langle V_{out}\rangle(V_{ac}, V_{dc})$, with V_{dc} being the fast axis, swept from negative to positive voltages. Both voltage axes were normalized in units of the critical voltage V_c, which was experimentally measured to be 0.73 V. The resulting I-V curves were then numerically differentiated, so that voltage plateaus result in dark blue regions of vanishing $\tilde{R}$, while yellow boundaries correspond to transitions between plateaus. The map bears a striking similarity to the patterns observed in a conventional overdamped Josephson junction under microwave radiation [25].

The phase dynamics of an AC-driven Josephson junction can be obtained analytically when it is voltage biased, a case where the dependence of the Shapiro steps on the AC bias can be expressed with Bessel functions [2,24]. In our case, the junction is current-driven, and no such analytical result exists. Figure 4(c) was generated by numerical integration of (1), and the same averaging procedures used for the experimental map in Fig. 4(b) were conducted. A more detailed derivation of the map in Fig. 4(c) is given in the Supplemental Material [16]. Thus, a comparison of Figs. 4(b) and 4(c) allows a comparison of theoretical predictions of a differential resistance map and

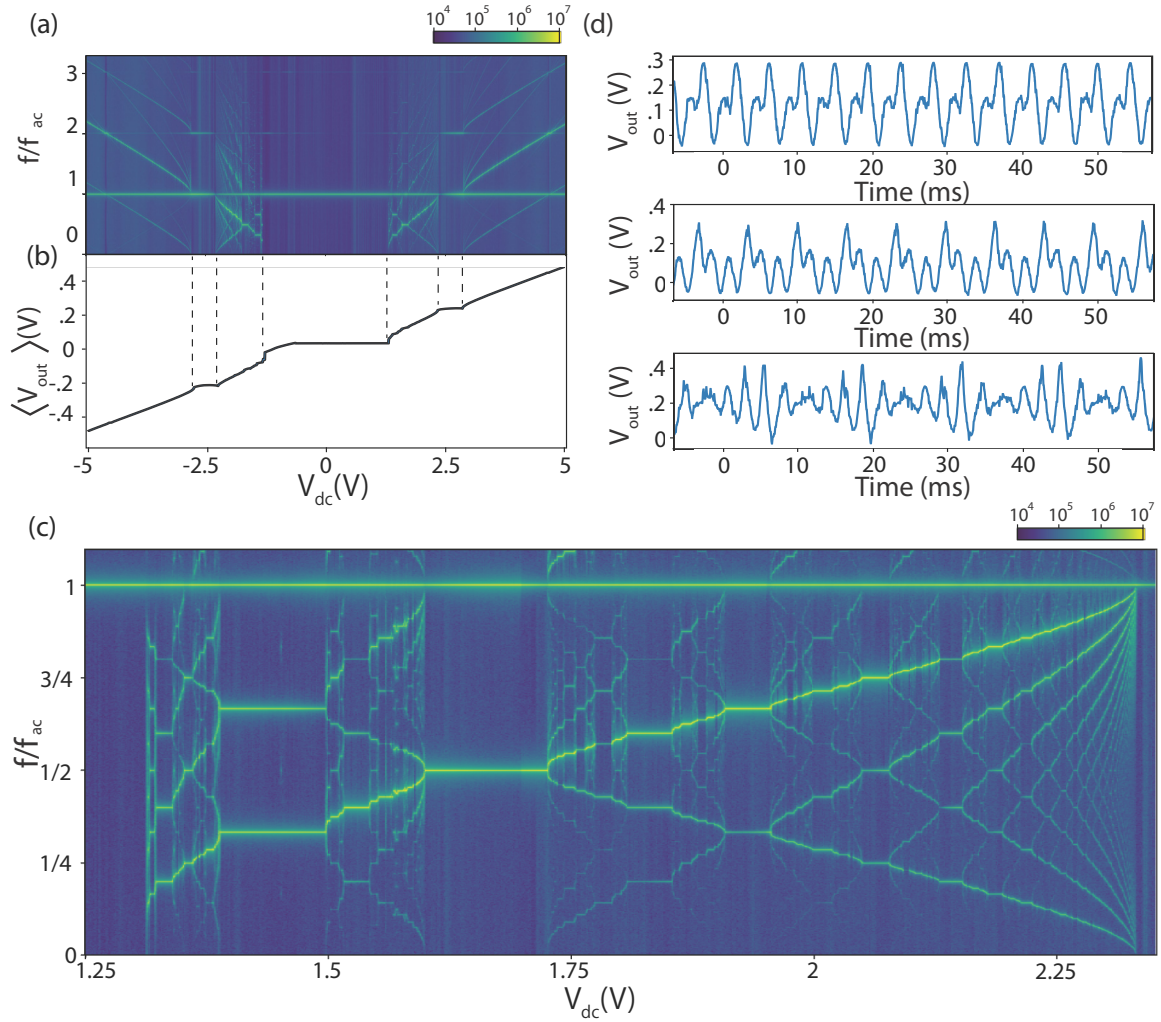

FIG. 5. Fractional Shapiro steps. (a) Spectral density of V_{out} as a function of V_{dc} obtained by fast Fourier transform. The junction is driven by an AC voltage $V_{\text{ac}} = 0.7V$. Frequencies are expressed in units of the external drive frequency $f_{\text{ac}} = 457$ Hz. The junction analog is tuned to the overdamped regime with $Q = 0.4$ and $f_0 = 410$ Hz. (b) DC response $\langle V_{\text{out}} \rangle$ measured over the same range of bias values. Vertical dashed lines are guides to the eye to identify phase-locked regions. (c) Detailed map of the spectral density of V_{out} as a function of V_{dc} between the $n = 0$ and $n = 1$ integer plateaus. Measured for input biases V_{dc} from 1.25 to 2.4 V. (d) Examples of unfiltered time traces $V_{\text{out}}(t)$ recorded for bias values that yield subharmonic phase locking at $f_{\text{ac}}/2$ ($V_{\text{dc}} = 1.65V$), $f_{\text{ac}}/3$ ($V_{\text{dc}} = 1.4V$), and $f_{\text{ac}}/5$ ($V_{\text{dc}} = 2.14V$).

the results of data collected by the analog circuit. The striking similarities between the maps verify the correspondence between theory and the circuit.

IV. SUBHARMONICS AND CHAOS

We now turn to the observation of subharmonic phase-locked states at fractional multiples of the drive frequency, when $\langle \dot{\phi} \rangle = \frac{p}{q}\omega$ and p and q are coprime. Such states have been observed both numerically [24,26–29] and in transport measurements [30,31]. The more robust of those states manifest themselves as plateaus in $\langle V_{\text{out}} \rangle(V)$ at fractional multiples of the voltage quanta f_{ac}/k. However, we find that a direct measurement of the frequency spectrum of $V_{\text{out}}(t)$ detects fractional phase locking much more sensitively.

We set the AC excitation amplitude and frequency and record the output frequency spectrum as a function of the bias V_{dc}. To that end, for each value of V_{dc}, we record a time trace $V_{\text{out}}(t)$ with 10^6 data points spread over 2000 to 4000 cycles of the drive. We then compute the fast Fourier transform (FFT) for that particular time trace. Repeating this procedure at each bias value allows us to generate a map of the spectral density as a function of f and V_{dc}, as shown in Fig. 5(a). Here, one vertical cross section of the map corresponds to the FFT of $V_{\text{out}}(t)$ at a given value of the bias. This map is measured for an analog Josephson junction with a Q factor of 0.4, at an AC frequency of 457 Hz, and with an AC amplitude of 0.7 V. Understandably, a strong peak in the frequency spectrum is seen at all biases at the fundamental drive frequency f_{ac}, as well as at the corresponding higher harmonics. The effective I-V curve $\langle V_{\text{out}} \rangle(V)$ is shown in Fig. 5(b) over the same range of DC bias. We observe $n = -1$, $n = 0$, and $n = +1$ integer phase-locked states, which correspond to regions of the frequency spectrum where a spectral weight is significant only at the drive frequency and its higher harmonics. In the region $|V_{\text{dc}}| > 2.5$ V, where the I-V curve exhibits what would be a conventional Ohmic behavior in a regular junction, $V_{\text{out}}(t)$ is modulated at a frequency that increases with DC bias and

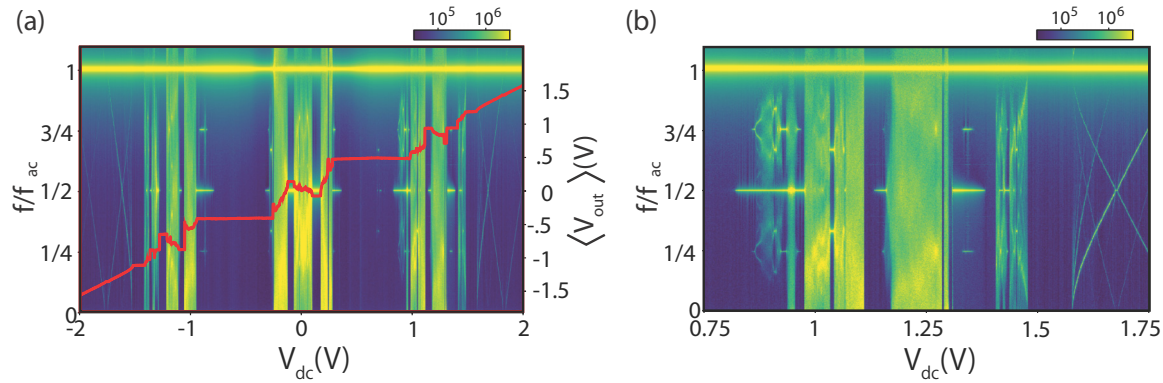

FIG. 6. Chaos in underdamped analog junctions. (a) Spectral density of $V_{\text{out}}(t)$ as a function of V_{dc} obtained by fast Fourier transform. An external AC drive $V_{\text{ac}} = 1.3$ V is applied. Frequencies are expressed in units of the external drive frequency $f_{\text{ac}} = 457$ Hz. The junction analog is tuned to the underdamped regime with $Q = 1.6$ and $f_0 = 470$ Hz. The DC response $\langle V_{\text{out}} \rangle (V_{\text{dc}})$ is superimposed over the map (in red). (b) Detailed map of the bifurcations between the $n = 1$ and $n = 2$ plateaus, using the same parameters.

is visible as a diagonal curve in Fig. 5(a). In this region of parameter space, the phase derivative is quasiperiodic and is not locked to the drive [24].

The region of parameter space between phase-locked states $n = 0$ and $n = 1$ exhibits a richer phenomenology and is shown in much greater detail in Fig. 5(c). A plethora of subharmonic phase-locked states are observed, as evidenced by steplike resonances in the FFT map. We show the corresponding time domain $V_{\text{out}}(t)$ in Fig. 5(d) for three of those subharmonics corresponding to $f_{\text{ac}}/2$, $f_{\text{ac}}/3$, and $f_{\text{ac}}/5$ (measured, respectively, at $V_{\text{dc}} = 1.65$ V, $V_{\text{dc}} = 1.4$ V, and $V_{\text{dc}} = 2.14$ V).

We observed subharmonic phase-locked states for both underdamped and overdamped analog Josephson junctions. However, they are easier to see for $Q < 1$ as they do not compete with chaotic states, and transitions between integer phase locked states in $\langle V_{\text{out}} \rangle (V_{\text{dc}})$ are less sharp, which leaves greater regions of parameter space where subharmonics are visible. Prior work showed that the I-V curve of a shunted Josephson junction at the onset of chaos forms a complete devil's staircase, a fractal of dimension $D \approx 0.86$ [26–28,32–34]. Our data are reminiscent of this fractal behavior. In particular, the main resonance that goes from the bottom left to the top right of the map in Fig. 5(c) is shown in greater detail in the Supplemental Material and shows stable plateaus at every rational number lower than 1 with a denominator up to ≈ 17 [16]. However, the resolution of the data set does not allow a satisfying determination of the fractal dimension. In the Supplemental Material, we show how solving Eq. (1) numerically can also provide the frequency spectrum of the phase and reproduce Fig. 5(c) with remarkable accuracy [16]. This confirms that the observed bias dependence of the frequency spectrum is, indeed, a dynamical effect predicted by the RCSJ model.

When the quality factor exceeds unity, $V_{\text{out}}(t)$ can exhibit chaotic behavior in addition to phase locking [24,26,33–45]. This is easier to see in the fast Fourier transform of $V_{\text{out}}(t)$: when it is chaotic, the spectral density is significant at all frequencies, so the FFT exhibits a large background as opposed to only a discrete number of peaks [6,35,37,44,45]. Figure 6(a) shows an example of a frequency spectrum measured as a function of the DC bias. The I-V curve $\langle V_{\text{out}} \rangle$ is superimposed in red on top of the map. Similar to Fig. 5, a resonance at f_{ac} dominates the spectrum of integer phase-locked states visible from $n = -2$ to $n = +2$. Between plateaus, green bands corresponding to a significant spectral density at all frequencies are visible and correspond to chaotic states. These bands are ubiquitous in those frequency spectrum maps as soon as Q exceeds 1 [24,35,43]. Transitions to chaos through period-doubling bifurcations [6] are clearly visible: they correspond to the emergence of subharmonics in the spectrum when the DC bias approaches a chaotic region (for example, slightly above $V_{\text{dc}} = -1$ V). Figures 6 and 5(c) also clearly depict intermittency. Such subharmonics appear in the spectrum before $\langle V_{\text{out}} \rangle$ starts deviating from a plateau value. This highlights the cascade of period-doubling preceding chaos, as the chaotic regions of the system are located within the jumps between plateaus. Figure 6(b) offers a more detailed view of a cascade of bifurcations in the frequency spectrum of the same analog junction, shown only between the $n = 1$ and $n = 2$ plateaus. We observe an alternation of period 2, period 4, and period 3 bifurcations as well as chaotic bands. In the Supplemental Material, comparable transitions between phase-locked and chaotic states are shown numerically [16].

Thermal noise in the AC-driven analog junction

Our experimental setup allows us to probe the stability of phase-locked and chaotic states in the presence of thermal noise.

We first discuss integer phase-locked states. The circuit is first tuned to a quality factor of approximately 0.6 and a junction frequency of 450 Hz. An AC bias is applied to the circuit at a frequency of 241 Hz, a large fraction of f_0. In what follows, the bias amplitude is fixed at a value of 1.35 V. The time-averaged output voltage of the circuit $\langle V_{\text{out}} \rangle$ then shows Shapiro steps as a function of the DC bias, as shown on Fig. 7(a).

In addition to the AC and DC biases, we apply a random voltage source of variable amplitude to the circuit. We again use the fact that the effective temperature corresponding to the noise source scales like V_{rms}^2. The resulting I-V curves

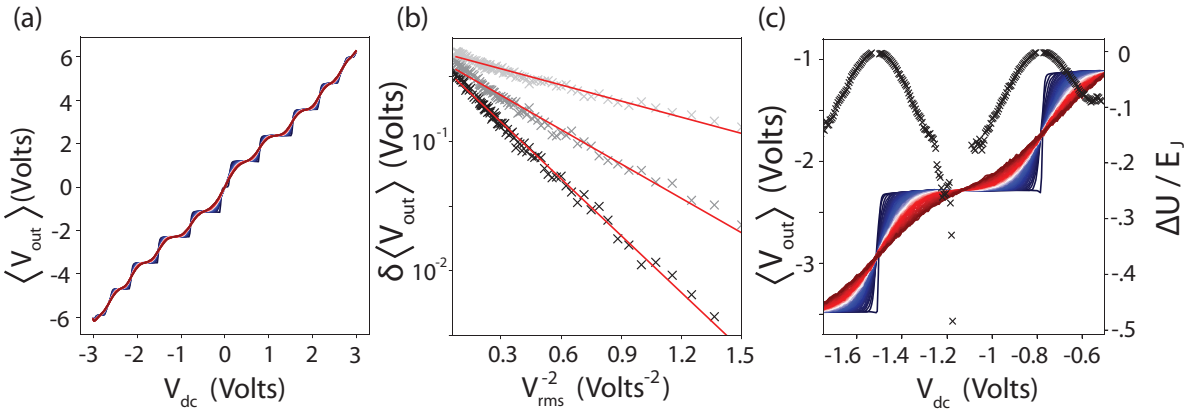

FIG. 7. (a) Plot of $\langle V_{out} \rangle$ as a function of the DC bias in the presence of an AC excitation at 241 Hz, $V_{ac} = 1.35$ V, and for thermal noise levels ranging from $V_{rms} = 0$ to $V_{rms} = 3$ V. (b) Arrhenius fit of the deviation from the plateau value δV represented in logarithmic scale as a function of V_{rms}^{-2}, which is proportional to $1/T$, measured at DC bias values increasingly close to the center of the plateau: $V_{dc} = -1.45$ V (light gray), $V_{dc} = -1.41$ V (dark gray), and $V_{dc} = -1.375$ V (black). (c) Activation energy as a function of bias (black).

are shown in Fig. 7(a) at different effective temperatures, ranging from zero to $V_{rms} = 3$ V. Transitions between plateaus become more rounded as the effective temperature increases.

The deviation from the plateau value δV is expected to be thermally activated as $\delta V \propto e^{-\Delta U/kT}$, where ΔU is the quasipotential quantifying the stability of the phase-locked state [24]. We thus plot the error voltage δV in logarithmic scale as a function of V_{rms}^{-2}, which is proportional to the inverse effective temperature [Fig. 7(b)]. The thermal activation behavior is evident from the linearity of the Arrhenius plot over more than one order of magnitude. That trend is represented for three different DC bias values ($V_{dc} = -1.45$, -1.41, and -1.375 V) at bias values that get closer to the center of the $n = 2$ plateau. The activation energy gets larger closer to the center of plateau, indicating an increased stability of the phase-locked state. We turn to a more systematic representation of the quasipotential ΔU as a function of the bias. Figure 7(c) represents the I-V curves $\langle V_{out} \rangle (V_{dc})$ at increasingly large effective temperatures (blue to red curves). This data set allows us to determine the activation energy scale ΔU as a function of the DC bias for a given phase-locked state. It is represented in black and in units of the Josephson energy for the circuit. One can see how ΔU, which quantifies the stability of the phase-locked state, vanishes at the boundaries of the plateau. Meanwhile, ΔU is largest at the center of the plateau, where the phase-locked state is most robust. Very close to the center of the plateau ($V_{dc} \approx -1.1$ V), the high temperature traces intersect the middle of the low-temperature plateau. The deviation δV therefore becomes vanishingly small even at high temperature, and it is therefore experimentally unfeasible to extract the energy scale ΔU for the few points closest to that plateau center. Finally, note that the quasipotential is expressed in units of the Josephson energy; the procedure we followed to make this conversion is detailed in the Supplemental Material [16]. The bias dependence of the quasipotential is consistent with theory [24], as well as our numerical simulations of Eq. (1) in the presence of both an AC drive and Gaussian white noise, which are shown in the Supplemental Material [16].

In the case of fractional phase-locked states the error voltage δV between low and high temperature is much smaller, which prevents us from obtaining a satisfying Arrhenius fit to $\delta V(T)$. We thus turn to a determination of the fast Fourier transform of $V_{out}(t)$ at different effective temperatures. Figure 8(a) represents this FFT as a function of the DC bias voltage V_{dc} and the frequency in units of f_{ac}. It is measured between the $n = 1$ and $n = 2$ Shapiro steps in a region of parameter space where numerous subharmonic steps are visible (the circuit is tuned so that $Q = 0.93$, $f_0 = 430$ Hz, and $f_{ac} = 457$ Hz). Similar to previous FFT maps, a resonance at the excitation frequency is visible in all maps, and additional resonances at rational multiples of f_{ac} indicate fractional phase locking. Three panels are measured at increasing effective temperatures, which are controlled by the rms amplitude of the voltage noise. We see how fractional resonances are smeared by thermal noise, with low denominator fractions being the most robust (the period-doubling resonance at $f_{ac}/2$ is the last to survive).

To better visualize the smearing of fractional phase-locked states, we show in Fig. 8(c) cross sections of the FFT as a function of frequency at two different effective temperatures. Cross sections are shown for subharmonics $f_{ac}/3$ and $f_{ac}/5$. The FFT are normalized so that the peak amplitude at the drive frequency has a weight of 1. Evidently, the background of the FFT rises with temperature, which causes the prominence of the FFT peak to drop with temperature. This prominence is shown as a function of thermal noise in Fig. 8(e). We defined the prominence as the average of the peak amplitudes of the FFT at multiples of f_{ac}/n, divided by the average of the background FFT value. This prominence is seen to drop with thermal noise, with a steeper drop for the larger denominator subharmonic ($n = 5$). This reflects the disappearance of the phase-locked state as the $V_{out}(t)$ becomes noisier.

We turn to the dependence of the chaotic bands on the thermal noise level. Similar to Fig. 8(a), in Fig. 8(b) we represent the FFT of $V_{out}(t)$ as a function of V_{dc} at different effective temperatures. Here, the circuit is tuned to be underdamped, with $Q = 1.6$, $f_0 = 470$Hz, $f_{ac} = 457$Hz, and $V_{ac} = 0.9V$, which allows for chaotic behavior to arise at certain bias values. As opposed to the fractional resonances, these chaotic bands do not depend on temperature within the range of applied noise levels. This distinction is most clear by com-

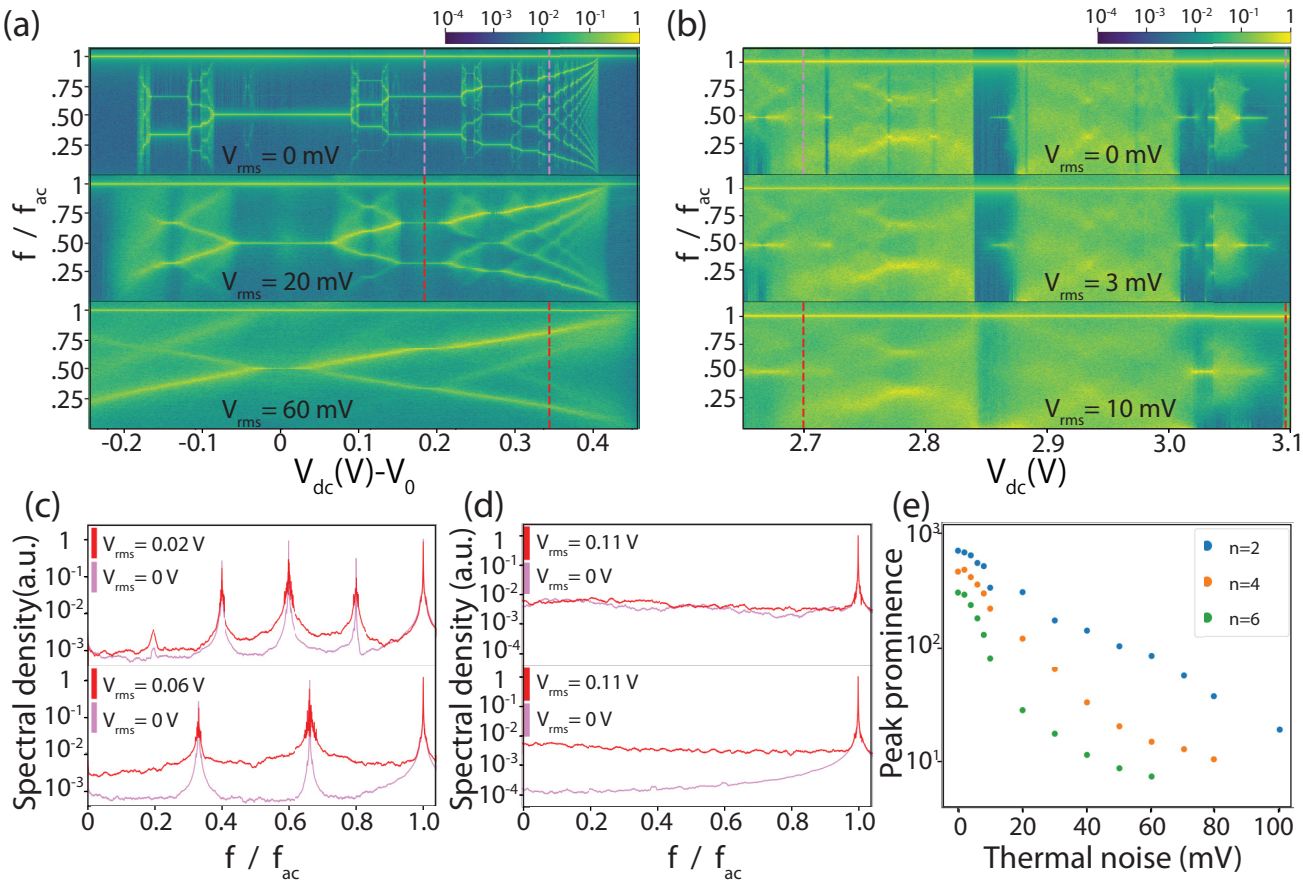

FIG. 8. Temperature dependence of chaos and subharmonics. (a) Spectral density of $V_{\mathrm{out}(t)}$ as a function of V_{dc} and frequency at three different temperatures. The junction is tuned to $Q = 0.93$ ($R = 330\,\Omega$) and $f_0 = 430$ Hz. Frequencies are expressed in units of the external drive frequency $f_{\mathrm{ac}} = 457$ Hz. These maps show how thermal noise smears subharmonic resonances. (b) Spectral density maps at three different effective temperatures in the underdamped regime with $Q = 1.6$, $f_0 = 470$, $f_{\mathrm{ac}} = 457$ Hz, and DC bias voltage swept from 2.65 to 3.1V. Notice how the background noise increases with temperature but leaves chaotic regions essentially unchanged. (c) Spectral density versus frequency line cuts of the subharmonic plateaus from (b). These more explicitly show the decreasing peak height and increasing background seen in (b). (d) Line cuts of chaotic maps from (b) showing spectral density versus frequency. For a phase-locked state (bottom panel, $V_{\mathrm{dc}} = 3.1$ V) the spectral density is relatively low at all frequencies except f_{ac} and its higher harmonics. As the noise level increases, so does the background of the spectral density, as expected. For a chaotic state (top panel, $V_{\mathrm{dc}} = 2.7$ V), the background of the spectral density is large even at zero temperature. It remains unaffected by the addition of thermal noise. (e) Peak prominence of subharmonic plateaus versus V_{rms} temperature. The prominences are measured as the ratio between the average peak height of the subharmonics and the background average.

paring how the phase-locked regions smear while the chaotic regions remain essentially unchanged. To illustrate this, we take cross sections of these maps in Fig. 8(d) just as we did for Fig. 8(c). The top map is taken in a chaotic region, and we can see that the background does not noticeably change at higher effective temperatures ($V_{\mathrm{rms}} = 0.11$V). This is in good agreement with prior numerical [6,35,37,44] and experimental work [31,45] that showed how the background spectral density in the chaotic regime vastly exceeds that of thermal noise at typical measurement temperatures. The bottom map was taken when only the fundamental frequency was present, and as temperature is increased, the background increases, which causes the prominence of the peak to drop.

Our results illustrate how this analog circuit replicates a wide range of Josephson junction phenomena. In the underdamped case, the retrapping voltage scales like the inverse of the quality factor, and the effective temperature dependence of the switching voltage distribution closely matches expectations from the RCSJ model. In overdamped junctions, we observe the diffusion of the phase in the presence of thermal noise. The addition of an AC excitation allows us to observe chaotic states, integer and fractional phase-locked states, and their dependence on AC power and temperature. This circuit paves the way toward the implementation of more complex analog circuits emulating the phase dynamics of driven multiterminal Josephson junctions [46–48], which have recently attracted a lot of interest due to the novel quantum and topological phenomena they can help engineer [49].

ACKNOWLEDGMENTS

We thank S. Teitsworth, E. Arnault, Y. Bomze, P. Richardson, T. Larsson, L. Zhao, and G. Finkelstein for helpful

discussions. S.I. and A.M. acknowledge funding from the Graduate Research Assistantship Mentoring Program and the Student And Faculty Excellence Fund at Appalachian State University.

[1] B. D. Josephson, Rev. Mod. Phys. **36**, 216 (1964).
[2] M. Tinkham, *Introduction to Superconductivity*, 2nd ed. (Dover, Mineola, NY, 1996).
[3] D. E. McCumber, J. Appl. Phys. **39**, 3113 (1968).
[4] W. C. Stewart, Appl. Phys. Lett. **12**, 277 (1968).
[5] C. A. Hamilton, Rev. Sci. Instrum. **43**, 445 (1972).
[6] D. D'Humieres, M. R. Beasley, B. A. Huberman, and A. Libchaber, Phys. Rev. A **26**, 3483 (1982).
[7] K. H. Gundlach, J. Kadlec, and W. Heller, J. Appl. Phys. **48**, 1688 (1977).
[8] J. H. Magerlein, Rev. Sci. Instrum. **49**, 486 (1978).
[9] A. Yagi and I. Kurosawa, Rev. Sci. Instrum. **51**, 14 (1980).
[10] R. W. Henry, D. E. Prober, and A. Davidson, Am. J. Phys. **49**, 1035 (1981).
[11] P. Russer, J. Appl. Phys. **43**, 2008 (1972).
[12] J. A. Blackburn, J. Appl. Phys. **101**, 093908 (2007).
[13] D. G. Luchinsky and P. V. E. McClintock, Nature (London) **389**, 463 (1997).
[14] S. W. Teitsworth, M. E. Olson, and Y. Bomze, Eur. Phys. J. B **92**, 74 (2019).
[15] S. Shapiro, Phys. Rev. Lett. **11**, 80 (1963).
[16] See Supplemental Material at http://link.aps.org/supplemental/10.1103/PhysRevB.104.184513 for details on the electronic circuit characterization, as well as additional numerical simulations of our results.
[17] H. Kramers, Physica (Amsterdam) **7**, 284 (1940).
[18] J. M. Martinis and R. L. Kautz, Phys. Rev. Lett. **63**, 1507 (1989).
[19] M. Büttiker, E. P. Harris, and R. Landauer, Phys. Rev. B **28**, 1268 (1983).
[20] P. Silvestrini, O. Liengme, and K. E. Gray, Phys. Rev. B **37**, 1525 (1988).
[21] M. H. Devoret, D. Esteve, J. M. Martinis, A. Cleland, and J. Clarke, Phys. Rev. B **36**, 58 (1987).
[22] J. Kurkijärvi, Phys. Rev. B **6**, 832 (1972).
[23] T. A. Fulton and L. N. Dunkleberger, Phys. Rev. B **9**, 4760 (1974).
[24] R. L. Kautz, Rep. Prog. Phys. **59**, 935 (1996).
[25] T. F. Q. Larson, L. Zhao, E. G. Arnault, M.-T. Wei, A. Seredinski, H. Li, K. Watanabe, T. Taniguchi, F. Amet, and G. Finkelstein, Nano Lett. **20**, 6998 (2020).
[26] M. H. Jensen, P. Bak, and T. Bohr, Phys. Rev. Lett. **50**, 1637 (1983).
[27] Y. M. Shukrinov, A. E. Botha, S. Y. Medvedeva, M. R. Kolahchi, and A. Irie, Chaos **24**, 033115 (2014).
[28] W. J. Yeh, D.-R. He, and Y. H. Kao, Phys. Rev. Lett. **52**, 480 (1984).
[29] E. Ben-Jacob, Y. Braiman, R. Shainsky, and Y. Imry, Appl. Phys. Lett. **38**, 822 (1981).
[30] J. Kuzník and K. Rogacki, Phys. Lett. A **176**, 144 (1993).
[31] M. Iansiti, Q. Hu, R. M. Westervelt, and M. Tinkham, Phys. Rev. Lett. **55**, 746 (1985).
[32] V. N. Belykh, N. F. Pedersen, and O. H. Soerensen, Phys. Rev. B **16**, 4860 (1977).
[33] M. H. Jensen, P. Bak, and T. Bohr, Phys. Rev. A **30**, 1960 (1984).
[34] T. Bohr, P. Bak, and M. H. Jensen, Phys. Rev. A **30**, 1970 (1984).
[35] R. L. Kautz and R. Monaco, J. Appl. Phys. **57**, 875 (1985).
[36] J. A. Blackburn, Y. Zhou-jing, S. Vik, H. J. T. Smith, and M. A. H. Nerenberg, Phys. D (Amsterdam) **26**, 385 (1987).
[37] B. A. Huberman, J. P. Crutchfield, and N. H. Packard, Appl. Phys. Lett. **37**, 750 (1980).
[38] N. F. Pedersen and A. Davidson, Appl. Phys. Lett. **39**, 830 (1981).
[39] W. J. Yeh and Y. H. Kao, Phys. Rev. Lett. **49**, 1888 (1982).
[40] D.-R. He, W. J. Yeh, and Y. H. Kao, Phys. Rev. B **30**, 172 (1984).
[41] E. G. Gwinn and R. M. Westervelt, Phys. Rev. Lett. **54**, 1613 (1985).
[42] M. Cirillo and N. Pedersen, Phys. Lett. A **90**, 150 (1982).
[43] R. L. Kautz, J. Appl. Phys. **52**, 6241 (1981).
[44] R. L. Kautz, J. Appl. Phys. **52**, 3528 (1981).
[45] R. F. Miracky, J. Clarke, and R. H. Koch, Phys. Rev. Lett. **50**, 856 (1983).
[46] A. W. Draelos, M.-T. Wei, A. Seredinski, H. Li, Y. Mehta, K. Watanabe, T. Taniguchi, I. V. Borzenets, F. Amet, and G. Finkelstein, Nano Lett. **19**, 1039 (2019).
[47] N. Pankratova, H. Lee, R. Kuzmin, K. Wickramasinghe, W. Mayer, J. Yuan, M. G. Vavilov, J. Shabani, and V. E. Manucharyan, Phys. Rev. X **10**, 031051 (2020).
[48] G. V. Graziano, J. S. Lee, M. Pendharkar, C. J. Palmstrøm, and V. S. Pribiag, Phys. Rev. B **101**, 054510 (2020).
[49] R.-P. Riwar, M. Houzet, J. S. Meyer, and Y. V. Nazarov, Nat. Commun. **7**, 11167 (2016).